

# Investigating Energy Bounds of Analog Compute-in-Memory with Local Normalization

Brian Rojkov, Shubham Ranjan, Derek Wright, Manoj Sachdev, *Fellow, IEEE*

arXiv:2602.08081v1 [cs.AR] 8 Feb 2026

**Abstract**—Modern edge AI workloads demand maximum energy efficiency, motivating the pursuit of analog Compute-in-Memory (CIM) architectures. Simultaneously, the popularity of large-language-models (LLMs) drives the adoption of low-bit floating-point formats which prioritize dynamic range. However, the conventional direct-accumulation CIM accommodates floating-points by normalizing them to a shared widened fixed-point scale. Consequently, hardware resolution is dictated by the input’s dynamic range rather than its precision, and energy consumption is dominated by the ADC. We address this limitation by introducing local normalization for each input, weight, and multiply-accumulate (MAC) output via a *Gain-Ranging MAC (GR-MAC)*. Normalization overhead is handled by low-power digital logic, enabling the computationally expensive MAC operation to remain in the energy-efficient low-precision analog regime. Energy modelling shows that the addition of a gain-ranging stage to the MAC enables a 4-bit increase in input dynamic range without increased energy consumption at a 35 dB SQNR standard. Additionally, the ADC resolution requirement becomes invariant to input distribution assumptions, allowing construction of an upper bound with a 1.5-bit reduction compared to the conventional lower bound. These results establish a pathway towards unlocking favourable energy scaling trends of analog CIM for modern AI workloads.

**Index Terms**—Compute-in-Memory (CIM), floating-point (FP), Mixed-Signal Circuits, Edge AI, Multiply-and-Accumulate (MAC)

## I. INTRODUCTION

COMPUTE-IN-MEMORY (CIM) architectures lead energy efficiency figures for the deep-neural-network (DNN) inference workload which increasingly dominates modern compute consumption [1]. Under the CIM paradigm, research has spanned architectural [2], [3], circuit [4], [5], and memory-device [6]–[9] domains. Nevertheless, practical implementations have largely converged on CMOS SRAM-based CIMs [10]–[21], owing to their combination of reliability, manufacturability, and favourable power-performance-area (PPA). The taxonomy in Fig. 1 categorizes prior art by computation domain, and quantization type.

Conventional integer CIM (INT-CIM) works (Fig. 1, *Uniform*) attain high energy efficiency by performing massive parallel computation in-situ, with techniques including digital bit-serial adder-trees to locally accumulate partial products [14], [15], or analog charge-domain accumulation one-shot physical dot-products [16], [17]. On the other hand, quantization literature has long recognized the information-efficiency

Compute-in-Memory (CIM)		
CMOS-SRAM	Analog	Digital
Uniform (INT)	[16],[17]	[14],[15]
Non-Uniform (FP)		[21]
FP → INT Conversion		
Mantissa-Alignment	[12],[13]	[10],[11]
FP-DAC/FP-ADC	[18]	
Addition-Only (Log-Domain)	[20]	[26]
Outlier-Aware		[19]
Fine-Grained Normalization	Proposed	

Fig. 1. Classification of CMOS-SRAM-based CIMs based on compute domain and quantization type. While emerging Non-Uniform/Floating-Point (*pink*) works offer superior information efficiency over Uniform/Integer (*blue*), prior implementations suffer from logic complexity, approximation, or overheads introduced by conversion and long-tailed data distributions. Our work (*bottom*) introduces a direct, native floating-point MAC to eliminate these bottlenecks.

advantage offered by floating-point formats, as independent control of range and precision allows the allocation of information across the format’s range to better match the distributions seen in neural network weights and activations [22], [23]. However, energy efficient floating-point CIM (FP-CIM) (Fig. 1, *Non-Uniform*) design remains a challenge, as the exponent breaks the inherent bit alignment structure which underpins the INT-CIM’s parallelism.

The prevailing solution, *mantissa-alignment*, forces compatibility by shifting mantissas by their exponents, effectively converting the data into a widened integer format suitable for conventional CIM arrays [10]–[13]. Unfortunately, this pre-processing incurs an energy overhead, and generates long-tailed data distributions with high bit sparsity, forcing the downstream INT-CIM array to overprovision for worst-case dynamic range, thereby wasting energy on redundant precision.

We propose adding a gain-ranging stage to the MAC to enable direct processing of normalized mantissas and provide a mechanism to reintroduce the exponent’s scaling during analog

Corresponding author: B. Rojkov (e-mail: brojkov@uwaterloo.ca)

The authors are with the Department of Electrical and Computer Engineering, University of Waterloo, Waterloo, ON, Canada.

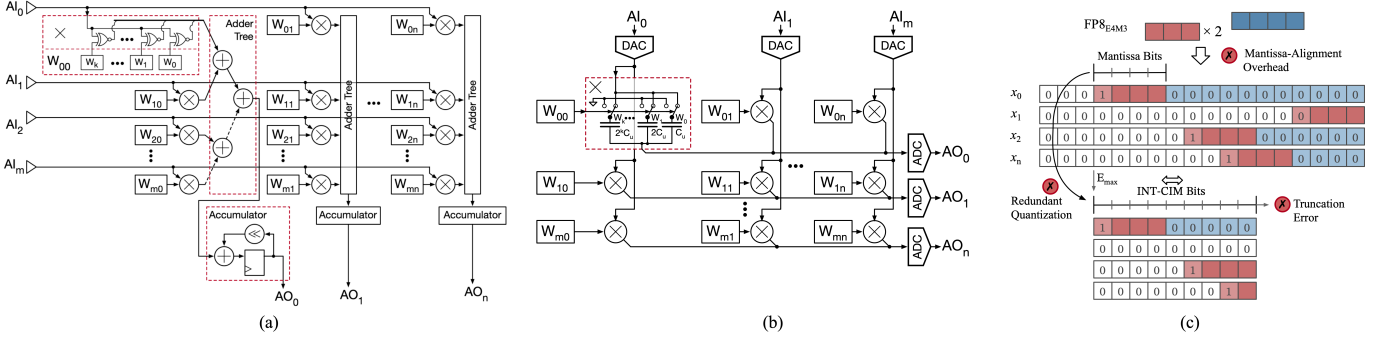


Fig. 2. Conventional CIM based on (a) digital and (b) charge-based analog techniques. (c) Global normalization procedure used to align floating-point inputs for processing in conventional CIM arrays.

accumulation. Our *Gain-Ranging MAC* (*GR-MAC*) provides the following benefits:

- 1) **Relaxed ADC Resolution:** Whereas the conventional CIM ADC resolution requirement depends on input data distribution assumptions, the proposed fine-grained normalization enables a data-invariant upper-bound on the required ADC resolution, reducing it by at least 1.5 bits, and over 6 bits under the empirically observed challenging conditions seen in LLMs.
- 2) **Favourable Energy Scaling Trends:** Increasing the useful input dynamic range of a conventional CIM requires a corresponding increase in the precision (input-referred signal-to-noise ratio) specification. The proposed technique decouples these metrics, allowing for an increased input dynamic range without the energy cost of higher precision data converters.

The benefit of low-bit floating point formats to LLM inference is to quantize high dynamic range data, without the overhead of high precision. The objective of this work is to provide a path to relay this benefit to CIM hardware. We quantify this by specifying the conventional and proposed CIM along independent dynamic range and precision axes and evaluate energy trends across this space in a design exploration study.

The rest of this paper is organized as follows. Section II reviews existing integer and floating-point CIM implementations. Section III proposes a mixed-signal FP-CIM architecture to serve as a platform for a design-space exploration. Section IV presents an analysis and discussion based on energy modelling. Finally, section V concludes this work.

## II. BACKGROUND

Fig. 1 provides an overall view of the CIM landscape reviewed in this section, making distinctions between compute domain, quantization type, and strategies for FP-CIM implementation. In this section, we will first review the operating principles and scaling limitations of INT-CIM architectures. Next, state-of-the-art FP-CIM architectures are reviewed to identify their specific merits and drawbacks.

### A. Conventional Integer CIM

Among many proposed analog and digital INT-CIM designs, the adder-tree-based digital CIM [14], [15] and capacitive-divider-based charge-domain analog CIM [16], [17] stand out in offering a combination of energy-efficiency and robustness.

1) *Digital CIM*: The digital CIM shown in Fig. 2 (a) operates by accumulating partial products within an adder tree integrated within the SRAM array [14], [15]. Distinct from standard memory access, wordlines are repurposed to function as single-bit activation inputs. These inputs trigger bit-wise multiplication with the stored weight data, generating partial products that enter the adder tree to be collapsed into a single dot-product result. The array operates in a bit-serial fashion, cycling through activation bits to shift and accumulate the partial outputs. This architecture minimizes data movement by resolving partial products of activations and weights directly within the memory cells, and immediately collapsing outputs in  $\log_2 n$  stages into a single accumulated dot-product. The digital CIM's energy efficiency is constrained by the dynamic switching of concurrent bitline readouts, the digital adder tree, and the accumulators. The digital INT-CIM's energy consumption scales quadratically with precision, as higher precision weights necessitate a proportional increase in accumulation logic, and higher precision activation inputs necessitate a proportional increase in bit-serial cycles, thus the compute energy mirrors the scaling of a conventional digital multiplier.

2) *Analog CIM*: To circumvent the digital CIM's high dynamic power cost, the analog CIM shown in Fig. 2 (b) replaces binary partial-product and accumulation logic with one-shot physical dot-product computation in the charge domain [16], [17]. By exercising a configurable network of capacitors, this architecture performs multiplication and summation directly in the charge domain. Capacitive dividers are interleaved into the SRAM array, where the locally stored weights configure the capacitor connections. DACs are the first step in the computation pipeline, driving voltages corresponding to a vector of activation inputs onto this capacitor network, allowing the dot-product to be computed through charge redistribution, before being digitized by an ADC for storage and further processing. However, it is this digital-analog-digital conversion overhead that bounds the system's efficiency. Unlike the quadratic  $N^2$

energy scaling of digital logic, the power consumption of a DAC and ADC scales exponentially with precision: following a  $2^N$  trend in the technology-limited regime, and steepening to  $4^N$  once thermal noise limits necessitate larger sampling capacitors [24]. Consequently, the viability of analog CIM is largely restricted to the low-precision domain, up to 8 bits [25], before exponential energy scaling eradicates the efficiency benefits of one-shot parallelism.

3) *Limitations of Integer CIM*: Despite their architectural distinctions, both digital and analog INT-CIMs share a limitation: the rigidity of the integer data format. To accommodate a required dynamic range  $DR$ , an integer format necessitates a bit-width of  $N \geq \log_2 DR$ . As established above, energy penalties scale aggressively, making it expensive to simply widen the integer format to capture outlier-heavy distributions. Furthermore, integer quantization enforces uniform resolution across the entire range, resulting in low information density for the various distributions typical of neural network weights and activations.

### B. Floating-Point CIM: Motivation, Approaches, and Challenges

Motivated by the limitations of integer formats, recent CIM research has pivoted toward floating-point formats, which offer a choice of exponent and mantissa bits to allocate information to a logarithmic and linear scale, respectively. This extra flexibility allows designers to choose a format more suited to the needs of their application. However, realizing this advantage in CIM hardware presents an implementation challenge, as the exponent breaks the bit-alignment structure that benefits INT-CIM architectures. Whereas integer bits hold fixed significance, the significance of a floating-point mantissa bit is variable and depends on its exponent. This prevents the direct in-situ accumulation of partial products common in integer arrays, forcing designers to adopt architectural workarounds that compromise the CIM's energy efficiency. Existing methodologies to address this challenge are discussed below.

1) *Distributed Digital Pipeline CIM*: One approach is to embed standard digital logic gates directly within the memory array, effectively distributing a digital multiplier pipeline across the SRAM rows [21]. This is a floating-point analogy to the digital adder-tree INT-CIM presented earlier. However, because the exponent and mantissa must be processed together, the INT-CIM's bit-serial scheme with direct readout of compact 10T SRAM bitcells is replaced with heterogeneous SRAM bitcells and periphery that collectively implement a full FP multiplier for each 8-bit weight cell. As a result, SRAM area comprises only 2% of the overall macro area and energy efficiency is  $5.5 \times$  worse compared to the same architecture's [21] shared-exponent mode which functions similarly to an INT-CIM with a shared scaling factor.

2) *FP→INT Conversion*: A popular strategy is to perform an FP-to-INT conversion to allow the use of a conventional INT-CIM for MAC operations [10]–[13], [18]. This is typically achieved through mantissa alignment [10]–[13]: first the maximum exponent within a data block is identified, and individual

values are denormalized by applying their exponent difference as a mantissa shift ( $M_i \ll E_{\max} - E_i$ ). This recovers the bit alignment property required for direct accumulation, thereby enabling INT-CIM techniques. However, this strategy introduces a new inefficiency compared to conventional digital FP logic. A standard FP multiplier maintains efficiency by processing the mantissa and exponent separately, using a compact multiplier sized for the normalized mantissa, and adders for exponents in the logarithmic domain. By contrast, after FP-to-INT conversion, the precision of the multiplier must be increased to fit the mantissa plus the range over which it may shift. This scales poorly with exponent bits due to the logarithm's compression: a digital multiplier's energy scales at  $N^2 \rightarrow (2^{E_{\text{bits}}})^2$  and analog data converters scale at up to  $4^N \rightarrow 4^{2^{E_{\text{bits}}}}$ . Due to the severity of this penalty, lower order bits are typically truncated, introducing a new energy-error tradeoff. Furthermore, the FP-to-INT conversion results in high bit sparsity, as most bit positions are occupied by 0s representing the mantissa's position rather than its information. This is inefficient for analog processing, as DAC and ADC hardware cost become dictated by the global dynamic range rather than active information content. To mitigate this, designers often adopt heterogeneous schemes to relax the precision requirements of the CIM array, such as redistributing sensitive MSBs to digital logic [12] or offloading outliers to an auxiliary digital core [13]. The compute overhead of mantissa alignment also introduces an energy bottleneck, for example, accounting for 39.8% of overall BF16 MAC energy in [10]. This is typically minimized by pre-aligning weight mantissas offline and storing the maximum weight exponent  $E_{\max,W}$ , as demonstrated in [10], [18]. However, runtime exponent normalization remains unavoidable for activation inputs. While an approach proposed by Y. Zhao et. al. [18] introduces an FP-DAC to eliminate the input mantissa shift, the fundamental mismatch between overall FP dynamic range and INT-CIM precision scaling persists. Finally, some CIM works segment multi-bit accumulation compute lines into multiple compute lines binned by bit-significance [18]; this lowers the peak ADC resolution requirement at the expense of additional conversions.

3) *Outlier-Aware*: S. He et. al. propose an outlier-aware quantization and CIM [19], where most weights and inputs are quantized to INT4 while reserving FP16 capability for a small number of outliers, by provisioning an array of configurable MACs: either operating on a single 16-bit FP16 input, or four 4-bit INT4 inputs. This approach imposes a structural requirement on input data, requiring that outliers make up no more than 3.125% of the overall data. Therefore, the INT4 format must accommodate 96.875% of the distribution. Additionally, configuring the MAC for an FP16 value requires pruning three adjacent INT4 values, although, the outlier-aware quantization algorithm demonstrates robustness to this noise for the OPT-1.3B-to-13B family of models.

4) *Addition-Only*: Another approach, the addition-only CIM [20], approximates floating-point multiplication by removing the second-order term of the mantissa product:  $(1.M_x \cdot 1.M_W) = (1 + M_x)(1 + M_W) = (1 + M_x + M_W + \cancel{M_x M_W})$ . The computationally expensive  $M_x \cdot M_W$  is removed, introduc-

ing a bounded error of at most  $1/4$ , and smaller than  $1/4$  in most cases. A similar concept is used in [26], replacing mantissa multiplication with addition for a logarithmic approximation of FP multiplication.

In summary, while the adoption of floating-point formats in CIM architectures offers improved information efficiency, fully realizing this potential in hardware remains constrained by the structural mismatch between variable exponents and fixed memory arrays. Prior implementations have addressed this by making compromises on (1) energy of distributed digital pipelines [21], (2) overheads and inefficiencies inherent to FP-to-INT conversion [10]–[13], [18], (3) structural limitations on input data [19], and (4) fidelity loss associated with approximation schemes [20], [26].

### III. AN ANALOG GAIN-RANGING MAC AND FP-CIM ARCHITECTURE

We propose a *Gain-Ranging MAC (GR-MAC)* to establish a new upper-bound on energy efficiency of the charge-based analog MAC and eliminate the structural mismatch between variable exponents and direct accumulation.

Figure 3 outlines the parameterized architecture for design space exploration. The mixed-signal CIM is organized as an array with  $N_R$  rows and  $N_C$  columns. Each row takes an  $N$ -bit floating-point input  $x$  (FP- $N_x$ , partitioned into  $N_{E,x}$  exponent and  $N_{M,x}$  mantissa bits), typically representing a neural network activation. The input's exponent is broadcast digitally, and the mantissa is distributed as an analog voltage via a DAC. Within the array, each unit cell packs  $N_Z$  FP- $N_W$  weight values in local SRAM, along with the switched-capacitor structures for charge-based MAC and an  $N_E$ -bit adder to compute the output exponent for gain ranging and normalization. The cell contributes its analog MAC output charge to its column's shared accumulation line, and a digital adder tree in each column accumulates the cell's output exponents encoded in a one-hot magnitude format ( $1 \ll E_i$ ) to determine the column's overall normalization factor. At the column periphery, the analog output is quantized by an ADC, which is then multiplied and normalized with the column normalization factor to obtain the final dot-product result. Optionally, the CIM array is wrapped in a global exponent normalization block to enable a wider input dynamic range than the CIM's native capability. Global normalization operates on the same principle as conventional FP-to-INT transfer CIMs [10]–[13], [18], but with an energy and fidelity overhead due to the additional compute and truncation.

#### A. Notation

We define the following conventions to facilitate our discussion and analysis. Boldface characters denote vectors and matrices (e.g., inputs  $\mathbf{x}$ , weights  $\mathbf{W}$ , pre-accumulation products  $\mathbf{p}$ , and pre-activation outputs  $\mathbf{z}$ ), while standard italics denote the scalar elements processed by individual unit cells and data converters (e.g.,  $x, W, p, z$ ). Signal variables are treated as dimensionless quantities normalized to the unit interval  $[-1, +1]$  for a signed signal and  $[0, 1]$  for an unsigned

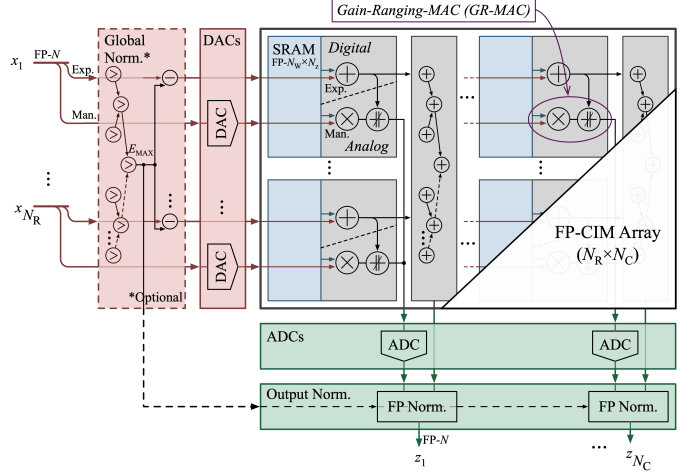


Fig. 3. The proposed Gain-Ranging MAC and CIM architecture template for design space exploration. Global normalization (dashed lines) is optionally included if more input dynamic range is required than the CIM array's native capability.

signal; physical values are easily obtained by scaling to a full-scale reference (e.g.,  $V_x = xV_{FS}$ ). To resolve ambiguity between overlapping terms, we distinguish the floating point exponent,  $E$ , from the energy consumption metric,  $\mathcal{E}$ . The stored components of a floating-point value are denoted as  $S$  (Sign),  $E$  (Exponent), and  $M$  (Mantissa). However, in the context of physical definitions,  $M$  and  $E$  denote the effective values rather than raw bit fields.  $M$  represents the significand normalized to the unit interval,  $M_x = 1.M_{x,\text{stored}}/2 \in [0.5, 1]$  for normals, and  $M_x = 0.M_{x,\text{stored}}/2 \in [0, 0.5]$  for subnormals). Likewise, the reserved code for subnormals is resolved for  $E$ ,  $E_x = \max(1, E_{x,\text{stored}})$ . Thus, the value of a floating-point scalar  $x \in [-1, +1]$  is easily written:  $x = (-1)^{S_x} \cdot M_x \cdot 2^{E_x - E_{\max}}$ .

#### B. The Gain-Ranging MAC (GR-MAC)

The charge-domain CIM array is a network of configurable capacitors that performs a Matrix-Vector Multiplication,  $\mathbf{z} = \mathbf{W}\mathbf{x}$ . The array is comprised of unit cells, each performing a single multiply-accumulate (MAC) operation. Each weight,  $W$ , is stored in a unit cell, and used to configure the local capacitive divider, thus embedding  $\mathbf{W}$  in the array. The input,  $\mathbf{x}$ , is applied across the rows of the array by DACs as voltages. Charge redistribution through the capacitive network generates the output voltages,  $\mathbf{z}$ , which are then quantized by ADCs at the column periphery. The ADC energy consumption scales with the required precision, ENOB, and becomes the primary energy bottleneck when scaling the charge-based CIM [25]. The ADC energy scaling is modeled as  $\mathcal{E}_{\text{ADC}} \propto \text{ENOB} + \gamma 4^{\text{ENOB}}$ , representing a linear baseline energy per conversion step, and a  $4^N$  term for thermal noise limited scaling, consistent with the SAR topology commonly used in CIM designs [27]. The crossover point between the two scaling regimes is defined by  $\gamma \approx N_{\text{cross}}/4^{N_{\text{cross}}}$  and  $N_{\text{cross}} \approx 10$  bits in [25], acting as a practical boundary for energy consumption.

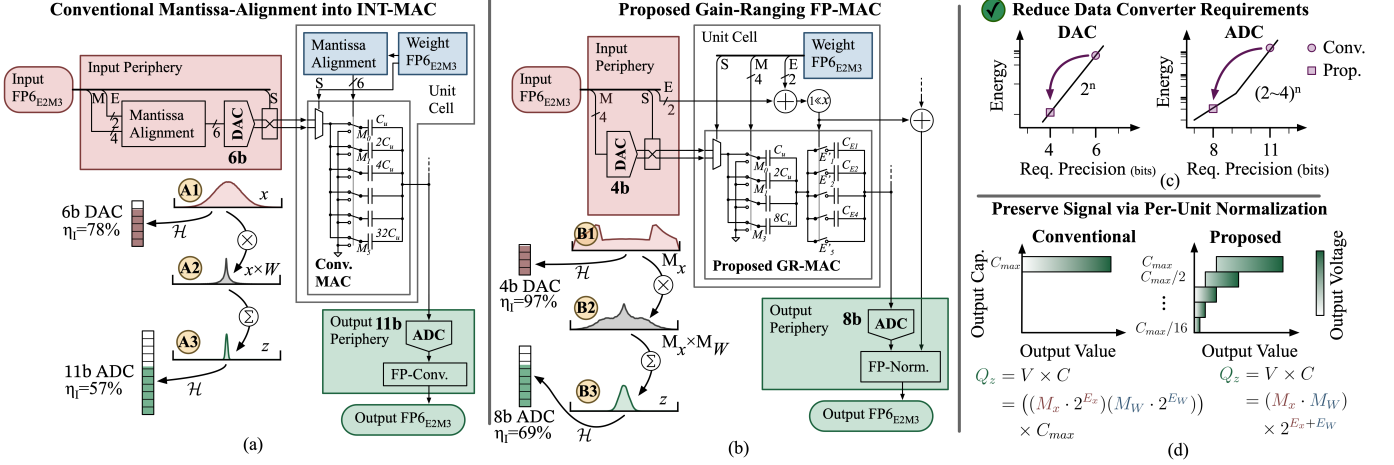


Fig. 4. (a) Conventional and (b) proposed MAC unit with periphery, enabling (c) a reduction in data converter precision, and (d) an illustration of the magnitude-based binning of normalization. The effect of redundant precision in the DAC and ADC required by conventional FP-to-INT architectures are shown as bars filled to represent the information content of the quantized inputs as a fraction of the capacity dictated by DAC and ADC requirements. A normal distribution clipped to  $4\sigma$  is chosen for the input  $x$  and weight  $W$  for illustration purposes; the proposed GR-MAC's benefit is not strictly reliant on this input distribution. Similarly,  $N_R = 32$  and the FP6 data format are chosen as an example for illustration. The ADC resolutions are specified according to the analysis in Section IV.

The following subsection, III-B1, explains how dot-product computation on data that is globally normalized to a block-wise maximum, such as an aligned integer format [10]–[13] or FP-DAC [18], produces a *signal shrinkage* [25] effect. This forces the ADC to satisfy an *excess resolution requirement* [25] to lower the noise floor to distinguish the compressed signal, at an energy cost up to  $4^N$ . By contrast, the GR-MAC leverages the separation of range and resolution in floating point formats to apply *per-unit normalization*. Subsection III-B2 explains the operation of the GR-MAC, showing how weighted accumulation via gain ranging replaces uniform averaging to minimize signal shrinkage, thereby relaxing the ADC requirements.

1) *INT-MAC and Signal Shrinkage*: The conventional multi-bit charge-based INT-MAC, shown in Fig. 4 (a), works by scaling the input voltage through a capacitive divider with a ratio configured by the weight, performing a local  $p_{i,j} = x_i \cdot W_{i,j}$ , which is connected to a shared column compute line for accumulation ( $z_j = 1/N_R \sum_{i=1}^{N_R} p_{i,j}$ ). The INT-MAC's output signal power is compromised by signal shrinkage due to the statistics of multiplication and accumulation under a fixed full-scale range. Since the output scale is fixed to accommodate the maximum product ( $1 \times 1$ ), the multiplication of fractional inputs ( $|x|, |w| \leq 1$ ) contracts the signal variance relative to the full-scale limit. Adopting a first-order model of uncorrelated, zero-mean inputs, this contraction is given by  $\sigma_p^2 = \sigma_x^2 \sigma_W^2$ , as illustrated in Fig. 4 (A1)  $\rightarrow$  (A2). Signal variance is further suppressed by accumulation; each MAC's output remains connected to the column compute line, physically realizing the accumulation as dividing each MAC's charge across the total lumped capacitance. While this inherent averaging accommodates the theoretical worst-case sum without saturation, variance further shrinks by the column depth,  $\sigma_z^2 = \sigma_{z,i}^2/N_R$ , as shown in Fig. 4 (A2)  $\rightarrow$  (A3).

Crucially for FP-to-INT architectures, this signal degra-

dation is compounded by resolution mismatch created by mantissa alignment during global normalization. By forcing local inputs to align with a block-wise global maximum, the required integer bit-width is set to accommodate a range of exponents, thereby demanding more accuracy than is strictly specified by the floating-point mantissa.

The ADC minimum energy bound is ideally set by the requirement to keep noise introduced by analog processing below the quantization noise floor inherent to the input's format. However, signal shrinkage introduced by the INT-MAC operation lowers signal power, demanding a likewise suppression of the noise floor to maintain the target SNR during output quantization. This is quantified as an excess resolution requirement, raising the ADC energy per conversion by a factor of up to  $4^{ENOB}$ . Additionally, the increased bit-width caused by FP-to-INT conversion increases the required precision of the input DACs and further attenuates the output signal according to the block-wise maximum of the input data. The next section explains the operation of the GR-MAC and showcases how per-unit normalization relaxes the ADC requirement.

2) *GR-MAC and Signal Preservation*: Floating-point formats offer a natural foundation to address this bottleneck, as range (DR) is no longer strictly tied to precision (SQNR), with  $N_E$  and  $N_M$  allowing for decoupled control of each. This decoupling eliminates the INT-MAC's requirement to pay for a high DR with large integer bit-widths, which previously inflated analog resources. Instead, the proposed GR-MAC leverages this inherent separation of range and resolution to apply *per-unit normalization*. This eliminates the need to compress the entire global dynamic range into the fixed voltage scale, and offloads the low-overhead exponent arithmetic to the digital domain.

The GR-MAC operation is shown in Fig. 4 (b). The multiplier functions similarly to the INT-MAC, with a digital weight

input configuring a capacitive divider to operate on an analog voltage activation input. However, the GR-MAC multiplier operates only on the normalized floating-point mantissas, (B1), instead of denormalized integer values, (A1). This produces a normalized output product, (B2), which cannot be directly distributed onto the column compute line because its exponent may differ from other outputs: this is the conflict which prevents direct-accumulation and why other architectures must denormalize inputs before multiplication. Instead, the GR-MAC introduces gain-ranging stage to enable *weighted accumulation*: outputs are shared scaled according to their exponent, by selecting a variable capacitive coupling to the column compute line as  $C_{\text{cpl}} \in \{C_{\text{tot}}, \frac{C_{\text{tot}}}{2}, \frac{C_{\text{tot}}}{4}, \dots, \frac{C_{\text{tot}}}{2^{E_{\text{max}}-1}}\}$ , where  $C_{\text{tot}} = (2^{N_{\text{M},W}} - 1)C_{\text{u}}$  represents the total capacitance of the mantissa multiplication stage and therefore the maximum available coupling capacitance. The switched capacitive coupling stage is digitally controlled, using a one-hot input computed as the sum of the input and weight exponents,  $1 \ll E_x + E_w$ . Coupling capacitors are sized to create the desired ratios, such that  $C_{E,i} \parallel C_{\text{tot}} \propto 2^{E_i}$ . While the conventional MAC's column compute line output is available purely in the voltage domain, as its charge is always scaled to a constant worst-case  $N_{\text{R}}C_{\text{tot}}$ , the GR-MAC column output capacitance varies, keeping the output voltage normalized for efficient ADC conversion. A digital adder tree sums the one-hot output exponents to obtain the total column capacitance: this is the overall scaling factor to which the column output is normalized after ADC conversion. The adder tree cycles once per MVM and operate on low-activity one-hot inputs; by contrast, a conventional bit-serial digital CIM architecture (Fig. 2 (a)) requires one cycle for each input bit position.

The following subsection explains how the GR-MAC preserves output signal to reduce the ADC's ENOB requirement, thereby improving energy efficiency. First, while the effect of multiplication ( $\sigma_{a \cdot b}^2 = \sigma_a^2 \sigma_b^2$ ) is unavoidable, floating-point normalization maximizes the input amplitude by definition. This effect is seen comparing the conventional integer input [A1] to the proposed mantissa input (B1), and leads to the wider product distribution in (B2) compared to (A2). While normalized inputs maximize the initial signal swing, the dominant source of shrinkage in the conventional INT-MAC is the accumulation stage, where uniform averaging suppresses variance by the column depth  $\sigma_z^2 = \sigma_{z,i}^2/N_{\text{R}}$ . The GR-MAC directly addresses this by replacing uniform averaging with exponent-weighted averaging. This advantage is quantified by replacing  $N_{\text{R}}$  with an effective number of contributors,  $N_{\text{eff}}$ , to govern shrinkage. Adopting the standard formulation for weighted samples, this is defined as  $N_{\text{eff}} = (\sum 2^{E_i})^2 / \sum 4^{E_i} \leq N_{\text{R}}$ . While the worst-case scenario ( $N_{\text{eff}} = N_{\text{R}}$ ) occurs only if all inputs and weights share the exact same exponent, practical data distributions exhibit significant variation. In these cases, the exponential weighting allows the largest signals to dominate the average, driving  $N_{\text{eff}} \ll N_{\text{R}}$ . The example conditions in Fig. 4 produce  $N_{\text{R}} = 32$  in (A3) and  $N_{\text{eff}} = 14.6$  in (B3), and combined with normalized inputs improves overall output signal power by 20 $\times$ , for a reduction in the ADC excess resolution requirement of  $\Delta\text{ENO}B = 2.2$  bits. This benefit is quantified across different formats and input conditions in

Section IV.

Overall, the benefit of the GR-MAC is summarized as overcoming the rigid coupling between dynamic range and efficiency inherent to conventional analog INT-MAC. By processing normalized signals, the architecture maximizes the utilization of available signal swing, thereby minimizing the excess resolution requirement that drives ADC energy.

### C. Architecture Flexibility and Parameterization

Different granularities of normalization may be chosen, varying the trade-off between maximizing signal amplitude and complexity of exponent processing. This section describes these options, and the digital components which handle exponent bookkeeping.

1) *Unit Normalization*: Up to this point, the GR-MAC is described according to per-unit normalization, where each cell's output capacitance is scaled as a function of both the input and weight exponents, and thus represents the most fine-grained normalization. Since each cell has a unique output exponent, an adder-tree is required for each column. Each unit cell also contains a digital adder and binary decoder to generate the output exponent and switch configuration for the gain-ranging stage. Finally, the dot-product output is produced by multiplying the column-compute-line voltage converted by the ADC with the column exponent sum produced by the adder-tree. The adder-trees and output multiplication and normalization are amortized over each column, by  $N_{\text{R}}$ , and the unit cell logic is not amortized. Unit normalization is most energy efficient when the baseline ADC resolution requirement is high. In Section IV, the efficiency crossover point is identified at  $N_{\text{M},x} \geq 6$  in 28 nm technology; scaling to advanced nodes would likely lower this threshold due to superior digital scaling. A further limitation of unit normalization is that the bounded dynamic range of the gain-ranging stage must accommodate the sum of the input and weight exponents.

2) *Row Normalization*: The normalization bookkeeping overhead can be significantly reduced by only applying normalization to the inputs at run-time. Since the output capacitance of each unit cell then depends only on the input exponent, the unit cell is greatly simplified; the local exponent adder is removed, and the exponent decoder serves an entire row instead of a single unit. Furthermore, only one exponent adder-tree is required for the entire CIM array, and its input bitwidth is reduced. The exponent decoder is amortized over each row, by  $N_{\text{C}}$ , the exponent adder tree is amortized over the entire CIM array, by  $N_{\text{R}} \times N_{\text{C}}$ , and column output multiplication and normalization is unchanged, amortizing over each column, by  $N_{\text{R}}$ . The weights may be either stored shifted at the expense of storage overhead [18], or shifted at run-time at the expense of logic overhead for exponent decoding and mantissa shift. Section IV shows that row normalization granularity is most energy efficient when the ADC operates well below the thermal noise limited scaling regime in 28 nm technology. Finally, as the entire dynamic range of the gain-ranging stage is allocated towards the input, row-normalization offers a higher input dynamic range ceiling compared to unit normalization.

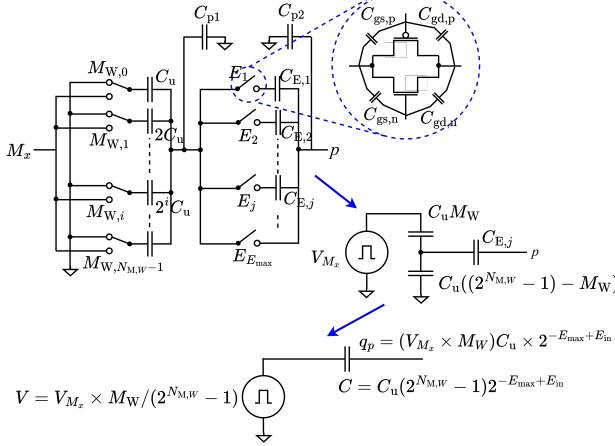


Fig. 5. Switched-capacitor divider with variable output capacitance used for GR-MAC. Switch and floating top- and bottom-plate parasitics are modeled to a first-order approximation as lumped capacitances  $C_{p1}$  and  $C_{p2}$  at the floating nodes.

3) *INT Normalization*: Integer inputs lack an exponent to provide scale information; however, if floating-point weights are used, a normalization benefit may still be obtained. Column exponent sums are pre-computed at compile-time, reducing digital logic to the bare minimum: an exponent decoder in each unit cell drives the switches in the gain-ranging stage, and a multiplier at each column output produces the final result.

#### D. GR-MAC Implementation Considerations

Although the proposed GR-MAC architecture, shown in Fig. 3, focuses on establishing theoretical limits of analog gain-ranging computation, physical realization of the circuit would face practical challenges similar to those in classical C-2C and binary-weighted DAC ladders. In particular, introducing a switched capacitive coupling stage to the output of a binary-weighted capacitor array leads to two key implementation concerns: (1) the need for non-multiple capacitor sizing to achieve the desired exponential gain profile, and (2) the introduction of parasitics due to floating top and bottom plates. Fortunately, both issues are well-studied in the context of C-2C DACs and compact capacitor array implementations, and several established techniques are applicable to GR-MAC design [16], [28], [29]. The main considerations are summarized below.

1) *Parasitic Capacitance Compensation*: As illustrated in Fig. 5, parasitic capacitances perturb the intended division ratio of the coupling network, degrading linearity and altering the gain boundaries between ranges. A well-known remedy in C-2C DACs [28], is to slightly enlarge the branch capacitors so that the effective division ratio, including parasitics, returns to an ideal  $1/2$  at each stage. In this approach, the branch capacitors are increased to  $\alpha C = C_p$ , absorbing the parasitic into the capacitor sizing, restoring the recursive halving condition. We similarly derive a closed-form expression for the required resizing of coupling capacitors in the GR-MAC, effectively cancelling the effect of  $C_{p1}$ , while  $C_{p2}$  is absorbed into overall

compute line capacitance and does not affect linearity:

$$C_{E_j} = \frac{(2^{N_{M,W}+1} - 1) C_u + C_{p1}}{2^{E_{\max}} - 1} \quad (1)$$

Because the correction depends directly on extracted parasitics, its effectiveness relies on accurate post-layout extraction. Prior work in INT-CIM macros demonstrates that this technique is sufficient to maintain linearity in 8-bit C-2C ladders fabricated in advanced FinFET processes [16]. The same methodology applies naturally to the GR-MAC's gain-ranging capacitive network, and a conservative limit of 6 bits is assumed for the analysis in Section IV.

2) *Arbitrary Capacitor Sizing*: The gain-ranging stage requires capacitor values determined by eq. 1, which generally cannot be realized using integer multiples of a unit capacitor. To accurately implement these non-integer ratios without introducing mismatch from fractional-unit structures, the unit-length scaling layout technique from [29] can be adopted. Since the capacitance scales linearly with metal length, this method enables fine-grained, monotonic tuning with resolution limited only by lithography, while preserving excellent matching and compact area.

## IV. ANALYSIS AND DISCUSSION

This section presents a design-space exploration to quantify the energy benefits which are obtained by adding gain-ranging to the analog MAC. We first analyze the ADC resolution, as the thermal-noise-limited regime boundary is the dominant scaling factor for CIM energy. Next, we use energy modelling to quantify the overall energy advantage of gain-ranging, incorporating the overheads introduced by the additional digital logic required for exponent bookkeeping for GR-MAC.

### A. ADC Requirements

To ensure robust analog processing of a given floating-point input, we restrict the permissible noise introduced by the ADC to 6 dB under the quantization noise floor of the input format, aligning with the findings in [25]. The relative error, and therefore SQNR of a floating-point format is related to the number of mantissa bits  $SQNR \approx 6.02N_M + 10.79$  dB [30], and is independent of the input data distribution, provided the data remains within the format's range. Although the format offers a bounded SQNR target, physical realization requires that the ADC noise floor decrease linearly with signal amplitude, which is data dependent. Thus, for a rigorous ADC specification it is necessary to consider both the SQNR requirement, and input data distribution, with particular consideration to long-tailed distributions which concentrate to small output amplitudes. We evaluate three distinct distributions, illustrated in Fig. 6 to define the hardware requirements:

- 1) *Uniform Distribution (baseline)* The uniform distribution is the standard baseline for conventional integer CIM analysis [25]. However, later in this subsection it is shown to underestimate the conventional CIM's ADC requirement for practical inputs.
- 2) *Maximum-Entropy Distribution* We consider the maximum-entropy distribution as the floating-point

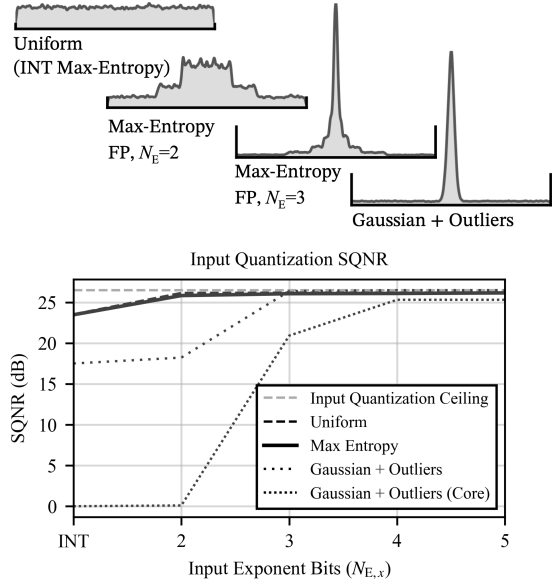


Fig. 6. Quantization noise vs exponent bits for the illustrated distributions. A floating-point format with  $N_M = 2$  is used. For visual clarity, the gaussian + outliers distribution is illustrated with an exaggerated gaussian core width and outlier probability.

equivalent of the uniform INT baseline. Defined as the distribution matching the quantizer prior, it can be obtained by uniformly randomizing the bits of a given format. This distribution is useful because it represents optimality in the choice of data format for a given workload; this is the explicit objective in some quantization works [31].

3) *Gaussian + Outliers Distribution (Empirical Dynamic Range Stress Test)* To model the activation patterns empirically observed in large language models [32]–[34], we construct this distribution as a mixture of a gaussian core with uniformly distributed high-magnitude outliers. This distribution is defined by the outlier probability,  $\epsilon$ , and magnitude,  $k$ , defined relative to the core’s  $3\sigma$ . It serves as a stress test for dynamic range: the hardware must resolve the narrow core without underflow, while simultaneously accommodating rare, massive outliers without clipping. For this analysis, we select values of  $\epsilon = 0.01$  and  $k = 50$ , consistent with empirical observations in [32]–[34] regarding the sparsity and magnitude of emergent features.

1) *Output-Referred Quantization Noise*: Fig. 6 illustrates the improvement in the SQNR which can be obtained by increasing the number of exponent bits for the considered distributions. The distributions which contain many large values quickly approach the SQNR ceiling because high-magnitude values dominate the global signal power; the transition from INT to  $FP_{E2}$  offers additional codes for a modest benefit, however, additional exponent bits offer little benefit, as the improved fidelity of small values is not captured by global SQNR. Herein lies the danger of using global SQNR to specify analog hardware for small core distributions with rare large outliers: this metric is dominated by even a small fraction of

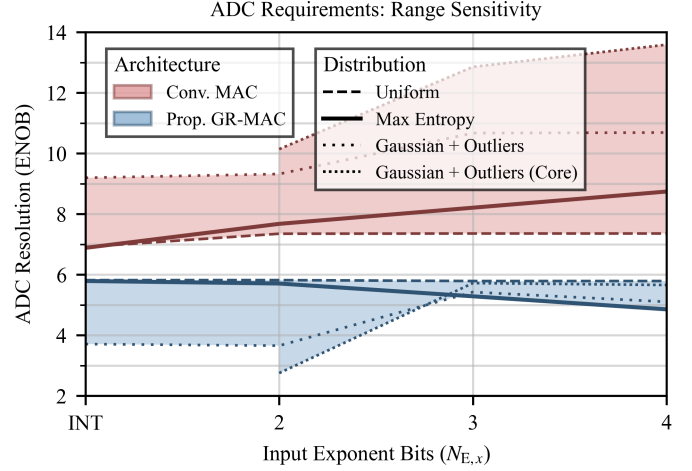


Fig. 7. Required ADC resolution, ENOB, as a function of input dynamic range, parameterized by exponent bits,  $N_{E,x}$ . The input format uses  $N_{M,x} = 2$  mantissa bits; sensitivity to input mantissa bits is minimal regarding range scaling trends, affecting ENOB by a constant offset (see Fig. 8). Weights are fixed to  $FP4_{E2M1}$ , and follow a maximum-entropy distribution, chosen as an information-optimal first-order approximation of empirical weights in [35]. The choice in weight format has negligible effect on output-referred SQNR since only input quantization noise is considered, and for accurate results needs only be sufficiently large to avoid sparse lattice artifacts in the output. ENOB is specified so as to exceed the output-referred SQNR by 6 dB for robust conversion.  $N_R = 32$  rows are used.

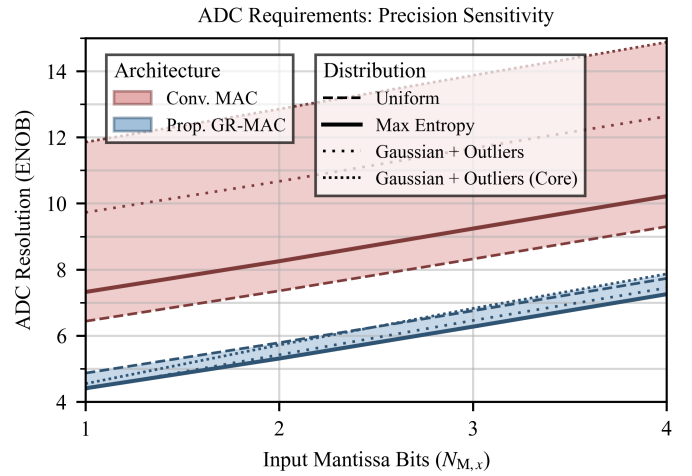


Fig. 8. Required ADC resolution, ENOB, as a function of input precision, parameterized by mantissa bits  $N_{M,x}$ . The input format uses  $N_{E,x} = 3$  so as to ensure that the studied distributions fall within the format’s dynamic range. As in Fig. 7, weights are fixed to  $FP4_{E2M1}$ , and follow the maximum-entropy distribution, and  $N_R = 32$  rows are used.

outliers and does not offer insight into the performance on the core distribution. This effect is particularly acute in the gaussian + outliers example which mimics the statistics of LLM activations. Therefore, it is instructive to also consider the SQNR on the subset of samples which do not contain outliers; this is shown in Fig. 6: ‘Gaussian + Outliers (Core)’. At  $N_{E,x} = 2$  the global SQNR is  $\approx 18$ , even though the core distribution containing the majority ( $\approx 99\%$ ) of the data produces no signal as it falls below the first quantization step’s rounding boundary. At  $N_{E,x} = 3$  the core distribution is resolved to within 6 dB of the ceiling, and SQNR plateaus

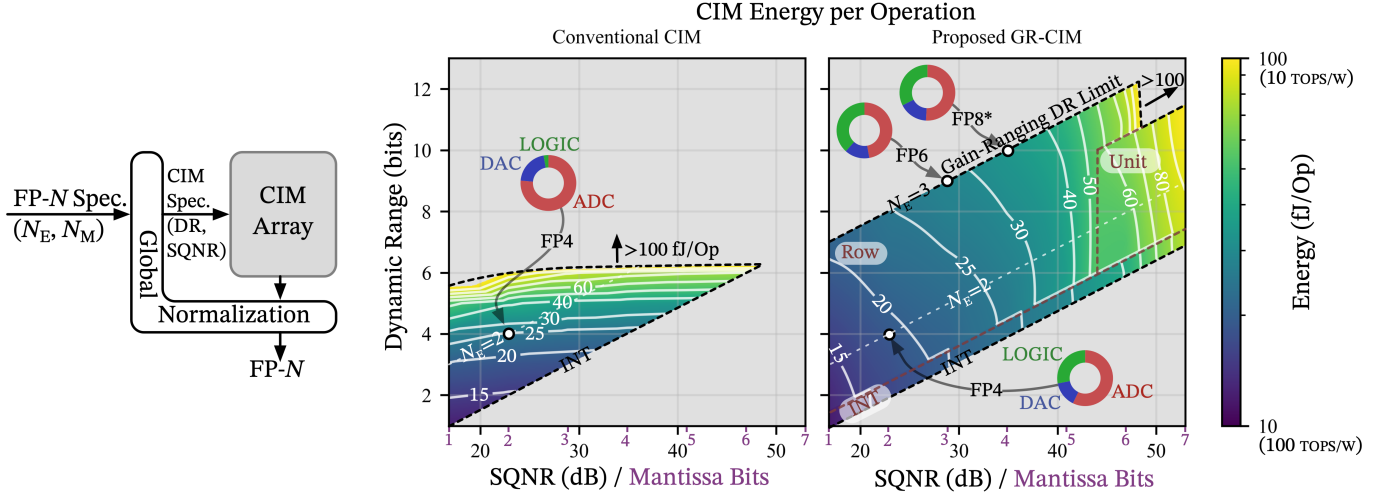


Fig. 9. CIM energy per operation according to input dynamic range (DR) and precision (SQNR) spec. The GR-MAC's normalization granularity may be INT, Row, or Unit (defined in Section III), and the energy-optimal regimes are annotated and delineated by dark-red dotted lines. Black or white dotted lines labelled INT,  $N_E = 2$ , and  $N_E = 3$  correspond to input formats with the specified number of exponent bits. Pie charts provide energy breakdowns for processing FP4, FP6, and FP8 inputs. FP4<sub>E2M1</sub> and FP6<sub>E3M2</sub> are shown natively without global normalization, while FP8<sub>E4M3</sub> requires global normalization to limit DR to a practical regime; only CIM array energy is included, as global normalization is independent of the CIM implementation. As the ADC specification is sensitive to the weight distribution prior but not the weight resolution, FP4 max-entropy weights are used, conforming to the previously established empirical observations and information-optimality assumption. A 32 × 32 CIM array is used. Each MAC is two operations. Mantissa bits include the implicit leading bit.

at  $N_{E,x} = 4$ .

2) *Range Sensitivity*: The required ADC resolution as a function of input dynamic-range, shown in Fig. 7, highlights the advantage of the proposed GR-MAC. The uniform distribution lower-bounds the conventional ADC ENOB requirement, as it presents the most efficient utilization of the full-scale range, but does not represent a practical workload, resulting in ADC underspecification. By contrast, gain-ranging introduced in the proposed architecture offers the least benefit under the uniform distribution, as the largest magnitude bins are most populated, and serves as a practical upper-bound which can be used for ADC specification. The proposed upper-bound demonstrates a 1.5 bit improvement over the conventional lower-bound. Moreover, as the input dynamic range increases to capture the gaussian + outliers core distribution ( $N_{E,x} \geq 3$ ), the ADC ENOB improvement of the proposed GR-MAC exceeds 6 bits. Crucially, the GR-CIM ADC resolution remains below the  $N_{\text{cross}} \approx 10$  bits thermal-noise-regime boundary for the ADC energy model defined in the Appendix. The ADC ENOB requirement is suppressed for the gaussian + outliers distribution at low  $N_{E,x}$ , due to the quantization fidelity as shown in Fig. 6.

3) *Precision Sensitivity*: The required ADC resolution scales linearly with the input format's precision, shown in Fig. 8, as the increased input precision creates a corresponding increase in ADC resolution. The 1.5-6 bit ENOB advantage of the proposed architecture is observed independent of the input resolution.

### B. Energy

The capability of the CIM array is specified by the input format it can robustly process, parameterized by dynamic

range (DR), and precision (SQNR). The energy per operation of the conventional CIM and proposed GR-CIM are modeled and compared across these dimensions. While a given SQNR corresponds directly to a minimum DR (i.e. the bitwidth of an INT format, for a uniform input), the objective of this work is to decouple these metrics, enabling an increased DR without requiring a corresponding increase in SQNR. For a floating-point format, the SQNR requirement is defined by the number of mantissa bits, while the additional DR is defined by the number of exponent bits.

For a given specification, the ADC is dimensioned to robustly ( $\text{SNR}_{\text{ADC}} \geq \text{SQNR}_x + 6$  dB) process a uniform input scaled to its narrowest valid bounds. This bound is defined as twice the minimum normal value, and represents the smallest range which is quantized to the target SQNR. Thus, the excess DR requirement beyond the minimum needed to achieve a given SQNR manifests as a relative shrinkage of the input signal amplitude with respect to the full-scale range, setting the ADC's worst-case resolution bound. The DAC is dimensioned under the same conditions: truncation is not performed as it would necessarily violate the SQNR specification, thus the DAC resolution increase for the conventional CIM matches the excess DR requirement, but remains constant for the proposed CIM, depending only on the SQNR requirement. The conventional CIM logic is specified to switch the capacitive dividers in each unit cell. In addition to switching the capacitor dividers, the proposed CIM provisions unit-cell exponent adders and decoders, exponent-adder trees, and multipliers for output normalization, depending on the normalization granularity, as defined in Section III. The energy models for the ADC, DAC, and digital logic components are described in the Appendix, together with the parameters for 28 nm.

Fig. 9 presents CIM energy per operation, contrasting the

scaling trends exhibited by the conventional and proposed CIMs. The valid design space is bounded along the ‘INT’ line by the minimum DR required to achieve a given SQNR. A practical upper-limit for energy of 100 fJ/Op (10 TOPS/W) is also used, which roughly coincides with the end of technology-limited ADC scaling under the parameters of this analysis. The GR-CIM’s efficient design regime is further bounded by the limited dynamic range of the gain-ranging stage; it is possible to increase dynamic range past this threshold, but only by scaling by the same manner as the conventional CIM.

The slopes of the energy contours indicate the relative cost of SQNR and DR throughout the design space: the ideal contour line is vertical, indicating that energy scales solely with precision, and allowing for increased input range without increasing energy consumption. A horizontal contour line indicates that the energy required to achieve a given range is dictated by the precision which achieves that range natively (along the INT line); thus, for a constant range, energy savings cannot be realized by reducing precision. This unfavourable DR-dominated scaling is demonstrated by the conventional CIM in Fig. 9. By contrast, the proposed GR-CIM exhibits SQNR-dominated scaling; increasing the required precision demands a corresponding increase in ADC energy according to well-known scaling trends [24], [36], while DR may be increased at the cost of additional normalization circuitry. In addition to favourable energy scaling, gain-ranging provides a constant benefit by normalizing inputs and weights, regardless of the DR requirement.

At the 100 fJ/Op limit, the GR-CIM can robustly process inputs with 6 bits more dynamic range than the conventional CIM, while maintaining the same SQNR (47 dB). Zhao et al. [18] state that 35 dB is sufficient for most Edge-AI applications; at this standard, the proposed GR-CIM achieves 4 bits more dynamic range for the same 30 fJ/Op energy cost.

For the common low-bit formats [37], at  $\text{FP4}_{\text{E2M1}}$ , the gain-ranging improves energy per operation by 23%. The  $\text{FP6}_{\text{E3M2}}$  format is outside of the practical range for the conventional CIM and would require global normalization adding additional energy cost and degrading fidelity, while the GR-CIM can process it natively at 29 fJ/Op. The large dynamic range of an FP8 format with  $N_{\text{E},x} \geq 4$  requires global normalization for either architecture. However, the proposed CIM extends the DR of the energy efficient regime by 6 bits compared to the fixed-point baseline. Consequently, when employed within a global normalization and segmentation scheme [18], the GR-CIM supports a significantly wider envelope per segment, minimizing segmentation overhead.

Fig. 9 also shows energy breakdowns, illustrating how the fine-grained normalization of the GR-MAC improves ADC energy, but incurs additional logic overhead. Moving forward to advanced nodes with more favourable digital scale is expected to reduce this overhead.

Overall, local normalization through the addition of gain-ranging to the analog MAC shows potential to significantly improve the energy and dynamic range envelope of the analog CIM.

## V. CONCLUSION

This work proposes adding a gain-ranging stage to the charge-based MAC to enable native analog processing of floating-point formats. Fine-grained normalization is shown to lower the ADC resolution requirement, enabling higher dynamic range inputs without global normalization or segmentation and the associated energy overheads and fidelity loss. Furthermore, an upper-bound is provided for the ADC specification, decoupling it from input distribution assumptions. Energy modelling shows that GR-MAC scaling is SQNR-dominated rather than dynamic-range-dominated, allowing for increased input dynamic-range at minimal energy cost. At a 35 dB standard, the GR-MAC enables a 4-bit increase in the input dynamic range without increased energy consumption. The GR-MAC provides guidance for the future role of analog compute for energy-efficient processing of AI workloads. Overall, these results support a broader trend of leveraging digital scaling to improve analog performance.

## APPENDIX

The analysis in this paper relies on models and parameters developed and validated by Sun et. al. in [27] against previously published analog and digital CIM implementations [10], [11], [13], [38]–[41]. They are summarized in Tables I and II and explained here.

TABLE I  
ENERGY MODELS FOR CIM COMPONENTS

Component	Energy
ADC	$(k_1 \text{ENOB} + k_2 4^{\text{ENOB}}) V_{\text{DD}}^2$
DAC	$k_3 \text{DAC}_{\text{res}} V_{\text{DD}}^2$
Cell array switching	$0.5 C_{\text{gate}} V_{\text{DD}}^2 N_{\text{SW}} N_{\text{R}} N_{\text{C}}$
Full Adder (FA)	$6 C_{\text{gate}} V_{\text{DD}}^2$
Adder Tree	$E_{\text{FA}} \cdot \# \text{FA}$
N-bit multiplier <sup>a</sup>	$(1.5 C_{\text{gate}} V_{\text{DD}}^2 + E_{\text{FA}}) N^2$
Binary Decoder <sup>a</sup>	$(0.5 N_{\text{in}} + N_{\text{out}} + 1) C_{\text{gate}} V_{\text{DD}}^2$

<sup>a</sup> Derived from [27] via standard logic scaling.

Definitions: ENOB: Effective ADC resolution,  $\text{DAC}_{\text{res}}$ : DAC resolution,  $N_{\text{SW}}$ : Number of switches per cell,  $N_{\text{R}}$ ,  $N_{\text{C}}$ : Number of rows and columns in the CIM array,  $N_{\text{in}}$ ,  $N_{\text{out}}$ : Decoder input and output bit-width.

TABLE II  
COST MODEL PARAMETERS @ 0.9 V, 28 NM

Parameter	Value
$C_{\text{gate}}$	0.7 fF
$k_1$	100 fF
$k_2$	1 aF
$k_3$	50 fF

- 1) **ADC:** The ADC energy model from [27] fits  $k_1$  and  $k_2$  according to empirical scaling limits (excluding outliers), consistent with [25], [36]. As explained in Section IV, the required ENOB is computed to ensure that the overall ADC  $\text{SNDR}_{\text{ADC}} \approx \text{SNR}_{\text{ADC}}$  exceeds the input SQNR referred to the ADC by a safety margin (6 dB), using

statistical simulations on various input conditions, rather than the closed-form solution proposed in [25] which is limited to signal shrinkage based on full-scale uniform inputs.

2) **DAC:** The DAC energy model proposed and validated in [27] models the energy cost according to  $k_3$ , a technology coefficient characterizing the effective switching capacitance per bit.

3) **Logic:**

- a) **Cell array switching:** This captures the total energy of bitline switching [27]. Each cell contains  $N_{SW}$  capacitor switches, each presenting a load of two transistors to the bitline. Accordingly, the cell capacitance, is normalized to  $0.5C_{gate}$ , where  $C_{gate}$  is the gate capacitance of a reference four-transistor NAND2/NOR2 gate. The proposed architecture introduces a gain-ranging stage, which increases  $N_{SW}$  by 1, as the one-hot encoded exponent control toggles once per operation.
- b) **Full adder (FA) and adder tree:** The energy of a full adder (FA) is modeled as  $6C_{gate}V_{DD}^2$ , accounting for the dominant internal node and output switching activity per addition [27]. This model is applied to the adder trees used for digital accumulation as well as unit-cell arithmetic used in the unit-normalization regime.
- c) **N-bit multiplier:** The energy of an N-bit multiplier is modeled as  $(1.5C_{gate}V_{DD}^2 + E_{FA})N^2$ , reflecting the quadratic scaling of the number of AND gates and FAs required to generate and accumulate partial products.
- d) **Binary Decoder:** The binary decoder controls the gain-ranging switched-capacitor array. Its energy is modelled as  $(0.5N_{in} + N_{out} + 1)C_{gate}V_{DD}^2$ , accounting for  $N_{in}$  inverters to generate complement signals, and  $N_{out}$  NAND gates and inverters, with the final inverters accounting for a constant  $(0.5 \cdot 2)$  as only two outputs toggle per cycle.

REFERENCES

- [1] N. Verma, H. Jia, H. Valavi, Y. Tang, M. Ozatay, L.-Y. Chen, B. Zhang, and P. Deaville, "In-Memory Computing: Advances and Prospects," *IEEE Solid-State Circuits Magazine*, vol. 11, no. 3, pp. 43–55, 2019.
- [2] J. Yue, Y. Liu, Z. Yuan, X. Feng, Y. He, W. Sun, Z. Zhang, X. Si, R. Liu, Z. Wang, M.-F. Chang, C. Dou, X. Li, M. Liu, and H. Yang, "STICKER-IM: A 65 nm Computing-in-Memory NN Processor Using Block-Wise Sparsity Optimization and Inter/Intra-Macro Data Reuse," *IEEE Journal of Solid-State Circuits*, vol. 57, no. 8, pp. 2560–2573, Aug. 2022.
- [3] R. Guo, X. Chen, L. Wang, Y. Wang, H. Sun, J. Wei, H. Han, L. Liu, S. Wei, Y. Hu, and S. Yin, "CIMFormer: A Systolic CIM-Array-Based Transformer Accelerator With Token-Pruning-Aware Attention Reformulating and Principal Possibility Gathering," *IEEE Journal of Solid-State Circuits*, vol. 59, no. 10, pp. 3317–3329, Oct. 2024.
- [4] J. Zhang, Z. Wang, and N. Verma, "In-Memory Computation of a Machine-Learning Classifier in a Standard 6T SRAM Array," *IEEE Journal of Solid-State Circuits*, vol. 52, no. 4, pp. 915–924, Apr. 2017.
- [5] A. Biswas and A. P. Chandrakasan, "CONV-SRAM: An Energy-Efficient SRAM With In-Memory Dot-Product Computation for Low-Power Convolutional Neural Networks," *IEEE Journal of Solid-State Circuits*, vol. 54, no. 1, pp. 217–230, Jan. 2019.
- [6] D. Ielmini and H.-S. P. Wong, "In-memory computing with resistive switching devices," *Nat Electron*, vol. 1, no. 6, pp. 333–343, Jun. 2018.
- [7] S. R. Sundara Raman, S. S. T. Nibhanupudi, and J. P. Kulkarni, "Enabling In-Memory Computations in Non-Volatile SRAM Designs," *IEEE Journal on Emerging and Selected Topics in Circuits and Systems*, vol. 12, no. 2, pp. 557–568, Jun. 2022.
- [8] Y.-H. Chiang, C.-E. Ni, Y. Sung, T.-H. Hou, T.-S. Chang, and S.-J. Jou, "Hardware-Robust In-RRAM-Computing for Object Detection," *IEEE Journal on Emerging and Selected Topics in Circuits and Systems*, vol. 12, no. 2, pp. 547–556, Jun. 2022.
- [9] Y. Halawani, B. Mohammad, M. Abu Lebdeh, M. Al-Qutayri, and S. F. Al-Sarawi, "ReRAM-Based In-Memory Computing for Search Engine and Neural Network Applications," *IEEE Journal on Emerging and Selected Topics in Circuits and Systems*, vol. 9, no. 2, pp. 388–397, Jun. 2019.
- [10] F. Tu, Y. Wang, Z. Wu, L. Liang, Y. Ding, B. Kim, L. Liu, S. Wei, Y. Xie, and S. Yin, "A 28nm 29.2TFLOPS/W BF16 and 36.5TOPS/W INT8 Reconfigurable Digital CIM Processor with Unified FP/INT Pipeline and Bitwise In-Memory Booth Multiplication for Cloud Deep Learning Acceleration," in *2022 IEEE International Solid-State Circuits Conference (ISSCC)*, vol. 65, Feb. 2022, pp. 1–3.
- [11] A. Guo, X. Si, X. Chen, F. Dong, X. Pu, D. Li, Y. Zhou, L. Ren, Y. Xue, X. Dong, H. Gao, Y. Zhang, J. Zhang, Y. Kong, T. Xiong, B. Wang, H. Cai, W. Shan, and J. Yang, "A 28nm 64-kb 31.6-TFLOPS/W Digital-Domain Floating-Point-Computing-Unit and Double-Bit 6T-SRAM Computing-in-Memory Macro for Floating-Point CNNs," in *2023 IEEE International Solid-State Circuits Conference (ISSCC)*, Feb. 2023, pp. 128–130.
- [12] P.-C. Wu, J.-W. Su, L.-Y. Hong, J.-S. Ren, C.-H. Chien, H.-Y. Chen, C.-E. Ke, H.-M. Hsiao, S.-H. Li, S.-S. Sheu, W.-C. Lo, S.-C. Chang, C.-C. Lo, R.-S. Liu, C.-C. Hsieh, K.-T. Tang, and M.-F. Chang, "A 22nm 832Kb Hybrid-Domain Floating-Point SRAM In-Memory-Compute Macro with 16.2-70.2TFLOPS/W for High-Accuracy AI-Edge Devices," in *2023 IEEE International Solid-State Circuits Conference (ISSCC)*, Feb. 2023, pp. 126–128.
- [13] J. Yue, C. He, Z. Wang, Z. Cong, Y. He, M. Zhou, W. Sun, X. Li, C. Dou, F. Zhang, H. Yang, Y. Liu, and M. Liu, "A 28nm 16.9-300TOPS/W Computing-in-Memory Processor Supporting Floating-Point NN Inference/Training with Intensive-CIM Sparse-Digital Architecture," in *2023 IEEE International Solid-State Circuits Conference (ISSCC)*, Feb. 2023, pp. 1–3.
- [14] Y.-D. Chih, P.-H. Lee, H. Fujiwara, Y.-C. Shih, C.-F. Lee, R. Naous, Y.-L. Chen, C.-P. Lo, C.-H. Lu, H. Mori, W.-C. Zhao, D. Sun, M. E. Sinangil, Y.-H. Chen, T.-L. Chou, K. Akarvardar, H.-J. Liao, Y. Wang, M.-F. Chang, and T.-Y. J. Chang, "An 89TOPS/W and 16.3TOPS/mm<sup>2</sup> All-Digital SRAM-Based Full-Precision Compute-In Memory Macro in 22nm for Machine-Learning Edge Applications," in *2021 IEEE International Solid-State Circuits Conference (ISSCC)*. San Francisco, CA, USA: IEEE, Feb. 2021, pp. 252–254.
- [15] V. Sharma, X. Zhang, N. S. Dhakad, and T. T.-H. Kim, "FlexDCIM: A 400 MHz 249.1 TOPS/W 64 Kb Flexible Digital Compute-in-Memory SRAM Macro for CNN Acceleration," *IEEE Transactions on Circuits and Systems I: Regular Papers*, pp. 1–12, 2025.
- [16] H. Wang, R. Liu, R. Dorrance, D. Dasalukunte, D. Lake, and B. Carlton, "A Charge Domain SRAM Compute-in-Memory Macro With C-2C Ladder-Based 8-Bit MAC Unit in 22-nm FinFET Process for Edge Inference," *IEEE J. Solid-State Circuits*, vol. 58, no. 4, pp. 1037–1050, Apr. 2023.
- [17] Y. Fu, W.-H. Yu, K.-F. Un, C.-H. Chan, Y. Zhu, M. Zhang, R. P. Martins, and P.-I. Mak, "FLEX-CIM: A Flexible Kernel Size 1-GHz 181.6-TOPS/W 25.63-TOPS/mm<sup>2</sup> Analog Compute-in-Memory Macro," *IEEE J. Solid-State Circuits*, pp. 1–11, 2024.
- [18] Y. Zhao, Y. Wang, R. P. Martins, C.-H. Chan, S. Yin, and M. Zhang, "A Hierarchical-Hybrid Floating-Point Compute-in-Memory Macro Using FP-DAC and FP-ADC for Edge-AI Devices," *IEEE Journal of Solid-State Circuits*, pp. 1–14, 2025.
- [19] S. He, H. Zhu, H. Zhang, Y. Ma, Z. Chen, M. Li, D. Zhai, C. Chen, Q. Liu, X. Zeng, and M. Liu, "A 22-nm 109.3-to-249.5-TFLOPS/W Outlier-Aware Floating-Point SRAM Compute-in-Memory Macro for Large Language Models," *IEEE Journal of Solid-State Circuits*, pp. 1–14, 2025.
- [20] W. Cao, J. Gao, X. Xin, and X. Zhang, "Addition is Most You Need: Efficient Floating-Point SRAM Compute-in-Memory by Harnessing Mantissa Addition," in *Proceedings of the 61st ACM/IEEE Design Automation Conference*. San Francisco CA USA: ACM, Jun. 2024, pp. 1–6.
- [21] J. Saikia, A. Sridharan, I. Yeo, S. Venkataramanah, D. Fan, and J.-S. Seo, "FP-IMC: A 28nm All-Digital Configurable Floating-Point In-

Memory Computing Macro," in *ESSCIRC 2023- IEEE 49th European Solid State Circuits Conference (ESSCIRC)*, Sep. 2023, pp. 405–408.

[22] A. Kuzmin, M. Van Baalen, Y. Ren, M. Nagel, J. Peters, and T. Blankevoort, "FP8 quantization: The power of the exponent," in *Proceedings of the 36th International Conference on Neural Information Processing Systems*, ser. NIPS '22. Red Hook, NY, USA: Curran Associates Inc., Nov. 2022, pp. 14651–14662.

[23] Y. Zhang, L. Zhao, S. Cao, S. Zhang, W. Wang, T. Cao, F. Yang, M. Yang, S. Zhang, and N. Xu, "Integer or Floating Point? New Outlooks for Low-Bit Quantization on Large Language Models," in *2024 IEEE International Conference on Multimedia and Expo (ICME)*, Jul. 2024, pp. 1–6.

[24] X. Tang, J. Liu, Y. Shen, S. Li, L. Shen, A. Sanyal, K. Ragab, and N. Sun, "Low-Power SAR ADC Design: Overview and Survey of State-of-the-Art Techniques," *IEEE Trans. Circuits Syst. I*, vol. 69, no. 6, pp. 2249–2262, Jun. 2022.

[25] B. Murmann, "Mixed-Signal Computing for Deep Neural Network Inference," *IEEE Transactions on Very Large Scale Integration (VLSI) Systems*, vol. 29, no. 1, pp. 3–13, Jan. 2021.

[26] M. Li, H. Zhang, S. He, H. Zhu, H. Zhang, J. Liu, J. Chen, Z. Hu, X. Zeng, and C. Chen, "A 19.7 TFLOPS/W Multiply-less Logarithmic Floating-Point CIM Architecture with Error-Reduced Compensated Approximate Adder," in *2024 IEEE International Symposium on Circuits and Systems (ISCAS)*, May 2024, pp. 1–5.

[27] J. Sun, P. Houshmand, and M. Verhelst, "Analog or Digital In-Memory Computing? Benchmarking Through Quantitative Modeling," in *2023 IEEE/ACM International Conference on Computer Aided Design (ICCAD)*, Oct. 2023, pp. 1–9.

[28] B. Razavi, "The R-2R and C-2C Ladders," *IEEE Solid-State Circuits Mag.*, vol. 11, no. 3, pp. 10–15, 2019.

[29] P. Harpe, "A Compact 10-b SAR ADC With Unit-Length Capacitors and a Passive FIR Filter," *IEEE J. Solid-State Circuits*, vol. 54, no. 3, pp. 636–645, Mar. 2019.

[30] B. Widrow and I. Kollár, *Quantization Noise : Roundoff Error in Digital Computation, Signal Processing, Control, and Communications*. Cambridge University Press, 2008.

[31] T. Dettmers, A. Pagnoni, A. Holtzman, and L. Zettlemoyer, "QLORA: Efficient finetuning of quantized LLMs," in *Proceedings of the 37th International Conference on Neural Information Processing Systems*, ser. NIPS '23. Red Hook, NY, USA: Curran Associates Inc., Dec. 2023, pp. 10 088–10 115.

[32] T. Dettmers, M. Lewis, Y. Belkada, and L. Zettlemoyer, "LLM.int8(): 8-bit matrix multiplication for transformers at scale," in *Proceedings of the 36th International Conference on Neural Information Processing Systems*, ser. NIPS '22. Red Hook, NY, USA: Curran Associates Inc., Nov. 2022, pp. 30 318–30 332.

[33] G. Xiao, J. Lin, M. Seznec, H. Wu, J. Demouth, and S. Han, "SmoothQuant: Accurate and efficient post-training quantization for large language models," in *Proceedings of the 40th International Conference on Machine Learning*, ser. ICML'23, vol. 202. Honolulu, Hawaii, USA: JMLR.org, Jul. 2023, pp. 38 087–38 099.

[34] J. Lin, J. Tang, H. Tang, S. Yang, G. Xiao, and S. Han, "AWQ: Activation-aware Weight Quantization for On-Device LLM Compression and Acceleration," *GetMobile: Mobile Comp. and Comm.*, vol. 28, no. 4, pp. 12–17, Jan. 2025.

[35] R. Banner, Y. Nahshan, and D. Soudry, "Post training 4-bit quantization of convolutional networks for rapid-deployment," in *Proceedings of the 33rd International Conference on Neural Information Processing Systems*. Red Hook, NY, USA: Curran Associates Inc., Dec. 2019, no. 714, pp. 7950–7958.

[36] B. Murmann, "ADC performance survey 1997-2025," 2025, [Online]. Available: <https://github.com/bmurmann/ADC-survey>.

[37] B. D. Rouhani, N. Garegrat, T. Savell, A. More, K.-N. Han, R. Zhao, M. Hall, J. Klar, E. Chung, Y. Yu, M. Schulte, R. Wittig, I. Bratt, N. Stephens, J. Milanovic, J. Brothers, P. Dubey, M. Cornea, A. Heinecke, A. Rodriguez, M. Langhammer, S. Deng, M. Naumov, P. Micevicius, M. Siu, and C. Verrilli, "OCP Microscaling Formats (MX) Specification," Open Compute Project, Tech. Rep., Date: 2023.

[38] I. A. Papistas, S. Cosemans, B. Rooseleer, J. Doevenspeck, M.-H. Na, A. Mallik, P. Debacker, and D. Verkest, "A 22 nm, 1540 TOP/s/W, 12.1 TOP/s/mm<sup>2</sup> in-Memory Analog Matrix-Vector-Multiplier for DNN Acceleration," in *2021 IEEE Custom Integrated Circuits Conference (CICC)*, Apr. 2021, pp. 1–2.

[39] J.-W. Su, Y.-C. Chou, R. Liu, T.-W. Liu, P.-J. Lu, P.-C. Wu, Y.-L. Chung, L.-Y. Hong, J.-S. Ren, T. Pan, C.-J. Jhang, W.-H. Huang, C.-H. Chien, P.-I. Mei, S.-H. Li, S.-S. Sheu, S.-C. Chang, W.-C. Lo, C.-I. Wu, X. Si, C.-C. Lo, R.-S. Liu, C.-C. Hsieh, K.-T. Tang, and M.-F. Chang, "A 8-b Precision 6T SRAM Computing-in-Memory Macro Using Segmented-Bitline Charge-Sharing Scheme for AI Edge Chips," *IEEE Journal of Solid-State Circuits*, vol. 58, no. 3, pp. 877–892, Mar. 2023.

[40] P. Chen, M. Wu, W. Zhao, J. Cui, Z. Wang, Y. Zhang, Q. Wang, J. Ru, L. Shen, T. Jia, Y. Ma, L. Ye, and R. Huang, "7.8 A 22nm Delta-Sigma Computing-In-Memory ( $\Delta\sum$ CIM) SRAM Macro with Near-Zero-Mean Outputs and LSB-First ADCs Achieving 21.38TOPS/W for 8b-MAC Edge AI Processing," in *2023 IEEE International Solid-State Circuits Conference (ISSCC)*, Feb. 2023, pp. 140–142.

[41] B. Yan, J.-L. Hsu, P.-C. Yu, C.-C. Lee, Y. Zhang, W. Yue, G. Mei, Y. Yang, Y. Yang, H. Li, Y. Chen, and R. Huang, "A 1.041-Mb/mm<sup>2</sup> 27.38-TOPS/W Signed-INT8 Dynamic-Logic-Based ADC-less SRAM Compute-in-Memory Macro in 28nm with Reconfigurable Bitwise Operation for AI and Embedded Applications," in *2022 IEEE International Solid-State Circuits Conference (ISSCC)*, vol. 65, Feb. 2022, pp. 188–190.